PHYSICAL REVIEW B **78**, 045108 (2008)

Local atomic and electronic structures around Mg and Al dopants in $LiNiO_2$ electrodes studied by XANES and ELNES and first-principles calculations

Kazuyoshi Tatsumi,[1,*] Yusuke Sasano,[1] Shunsuke Muto,[1] Tomoko Yoshida,[1] Tsuyoshi Sasaki,[2] Kayo Horibuchi,[2]
Yoji Takeuchi,[2] and Yoshio Ukyo[2]
[1]*Department of Materials, Physics and Energy Engineering, Nagoya University, Chikusa-ku, Nagoya 464-8603, Japan*
[2]*TOYOTA Central R&D Laboratories, Nagakute, Aichi 480-1192, Japan*

(Received 10 March 2008; revised manuscript received 13 June 2008; published 16 July 2008)

We investigated the local atomic and electronic structures around the dopants Mg and Al in a $LiNiO_2$-based cathode material by the combination analysis of their *K* shell electron energy-loss near-edge structures, x-ray absorption near-edge structures, and first-principles calculations. The occupation sites of the dopants in initial and cycled samples were examined. On the basis of the atomic structures and chemical bonding states of the models whose theoretical spectra were most consistent with the experimental spectra, we discussed the effects of Al and Mg on Li diffusion and their roles in suppressing the degradation of battery properties.

DOI: 10.1103/PhysRevB.78.045108 PACS number(s): 71.23.−k, 78.40.Pg, 61.50.Ah, 82.47.Aa

I. INTRODUCTION

$LiNiO_2$ is among the alternatives for $LiCoO_2$ as a cathode active material for lithium ion batteries because of its high specific capacity, low cost, and low toxicity. Its main drawbacks are the short lifetime of its electrochemical properties (capacity and resistance) due to the charge-discharge cycles and the safety problem due to the exothermic reactions associated with the structural instability of Li_xNiO_2 in its charged state ($x \sim 0.5$). In order to overcome these problems, multiple substitutions of nontransition-metal elements for the cation sites have been considered, small amounts (~a few at. %) of Mg,[1–7] Al,[8–18] and both[19–22] dopings being commonly reported to improve the cycle performance. Although the effects of the dopants have been discussed intuitively,[1,2] changes in the chemical bonding states of the near neighbor ions associated with the doping have not yet been examined in detail. In fact, x-ray diffraction analyses including the Rietveld refinements have estimated the dopant occupancies, which resulted in significant varieties,[1–5] partly depending on the differences in sample preparation conditions. A more direct method reflecting the dopant states is thus desirable because the x-ray Rietveld analysis is sensitive only to the numbers and spatial distributions of electrons in given structures/symmetries.

It is not so easy in terms of the total energies of the system calculated by first-principles calculations to determine which specific sites the dopant preferentially occupies because the procedure first requires the calculation of the total energies of several representative systems containing Ni at different oxidation states within accuracies of less than 0.1 eV/atom, in which the strong Coulomb repulsion between the Ni 3*d* electrons must be taken into consideration. This scheme seems beyond the limitations of the calculations based on the density-functional theory (DFT) because the accuracy required in calculating the total energy of the systems is higher than at the level where the DFT could correct its wrong evaluation of the Coulomb repulsion of Ni 3*d* electrons at each different site in the systems, through, for example, introducing an adjusting parameter called Hubbard *U*, which is defined as an effective on-site Coulomb interaction between the localized electrons in the system, representing an energy cost to remove and to add one localized electron, i.e., the ionization energy and the electron affinity. The error in the calculated solution energy due to the choice of the *U* value is comparable to the solution energy difference among the occupation sites. Several successful attempts have been made so far on these materials, mainly for the calculations of the average lithium intercalation voltages, which required no such complicated and sophisticated scheme.[23–27]

The combination of the experimental spectroscopic information and first-principles calculations is an effective alternative to investigate the local structures around the dopants. A promising spectroscopic technique for specifying the dopants' occupation sites would be core electron excited spectra of the dopants, such as x-ray absorption near-edge structures (XANESs) or electron energy-loss near-edge structures (ELNESs), since these structures directly reflect the local environments of the dopants.

The present study aims to explore the local atomic and electronic structures around the Mg and Al dopants in a $LiNiO_2$-based positive electrode material by the combination method mentioned above. Since the near-edge structures provide the electronic partial density of the unoccupied states of the dopants, first-principles electronic structure calculations can bridge the spectral fine structures and the local atomic and electronic structures of dopant sites.

II. EXPERIMENT AND CALCULATION

A. XANES/ELNES measurements

We studied the positive electrode active material $LiNi_{0.75}Co_{0.15}Al_{0.05}Mg_{0.05}O_2$, which is expected for use at relatively elevated temperatures. A powder sample was synthesized by the standard coprecipitation method.[19,28] The positive electrodes were fabricated from the $LiNi_{0.75}Co_{0.15}Al_{0.05}Mg_{0.05}O_2$ powder, conductive graphite, and polyvinylidene floride (PVDF) binder, coated on 20-μm-thick aluminum sheets. Some of positive electrodes were assembled into cylindrical cells together with artificial graphite as a negative electrode, and 1*M* $LiPF_6$ was dissolved in an electrolyte solution of ethylene carbonate and diethyl carbonate. The cycle properties at elevated temperatures were actually improved as compared to the cells with positive electrodes without Mg.[19,28] After 500 charge/discharge cycle tests at 60 °C, the cells were disassembled again to remove the degraded electrodes in argon atmosphere in a glovebox. The x-ray diffraction pattern of the sample after the cycling test showed no impurities, changes in the lattice constants, or peak broadening, either. The capacity and internal resistance were actually degraded by the cycling, the details of which have been reported elsewhere.[19,28] The electrodes were punched into 3 mmϕ disks, followed by conventional Ar-ion milling to obtain thin areas transparent to high-energy electrons.

Mg *K* XANESs were obtained from the as-synthesized powder and the electrodes after the cycle tests: XANESs were recorded in a total electron yield mode with a Beryl two-crystal monochromator at BL1A of the UVSOR, Institute for Molecular Science, Okazaki, Japan. Al *K* XANES was also obtained using a $KTiOPO_4$ (KTP) monochromator at the same beamline. The energy width of the monochromatized beam was 0.5–0.6 eV. Al *K* XANES was collected only from the initial powder because the energy range of Al *K* had beam intensities 1 order of magnitude lower and background intensities significantly larger than that of Mg *K* did, despite the electrode sample had a smaller surface areas than the powder.

Since XANES at these low energies collects spatially averaged and surface-localized information, we conducted electron energy-loss spectra (EELS) measurements from the electrodes before and after the cycling tests using a JEOL JEM200CX transmission electron microscope (TEM) operated at 200 kV with a LaB_6 electron source, equipped with a Gatan electron energy-loss (EEL) spectrometer, Enfina1000. The ELNES data were collected in the imaging mode without an objective aperture to earn signal intensities, under which condition most of the ELNES signals were caused by the dipole transitions. We probed transitions to states with angular-momentum number change $\Delta l = \pm 1$ of the core state, i.e., the Al and Mg unoccupied *p* orbital density of states (DOS). Small other contributions to the ELNES such as the monopole transition could be ignored because, as will be described later in Sec. III A, Mg *K* ELNES of the electrode had a very similar profile to that of XANES where other than the dipole contribution was negligible. The dispersion setting was 0.1 eV/channel and the energy resolution was about 1.1 eV full width at half maximum (FWHM) of the zero-loss peak. The pre-edge background of the raw data was removed using the power law, while the plural scattering was not removed because their intensities did not significantly affect the spectral features near the edge threshold. It should be noted that no appreciable radiation damages associated with the high-energy electron beam were observed during the measurements.

B. Theoretical calculations

For theoretical interpretation of the experimental spectra and further analysis of the chemical bonding changes caused by the dopants, first-principles calculations were performed within the framework of the generalized gradient approximation (GGA) (Ref. 29) in the DFT which partly included a Hubbard-type orbital-dependent interaction (GGA+U). In the GGA+U case, we used the spherically average version of Hubbard U (Refs. 30 and 31) for the Ni *d* states. The total energy is represented by

$$E_{\mathrm{GGA}+U} = E_{\mathrm{GGA}} + \frac{U-J}{2}\sum_{m,\sigma}(n_{m,\sigma} - n_{m,\sigma}^2), \tag{1}$$

where $n_{m,\sigma}$ is the occupation number of the *m*th *d* state of spin σ. $U-J=U_{\mathrm{eff}}$ was set to 6.7 eV, which was obtained by a self-consistent linear-response procedure.[24]

We used a $3\times3\times3$ supercell of the primitive cell of $LiNiO_2$, containing 108 atoms with a single dopant atom at a Li or Ni site at one time. Co was not taken into account for simplicity; the chemical bonding changes caused by the dopants would be qualitatively similar irrespective of the presence of Co. Rather, the replacement of a transition-metal (TM) site by an *sp* element would cause much larger changes. The effects of codoping of Mg and Al were not considered either.

Prior to the spectral calculation, a low-energy atomic arrangement due to the dopant substitutions was obtained with GGA and GGA+U, using the projected augmented wave method,[32,33] as implemented in the Vienna *Ab-initio* Simulation Package.[34] In these calculations, a cutoff energy of 400 eV and a $2\times2\times2$ **k**-point mesh were used. The atom positions were freely relaxed under the constraint of the given symmetry of the supercell within the fixed supercell size until the residual forces were reduced to less than 0.05 eV/Å. We tested the optimization of all parameters including lattice vectors, however, the resultant atomic arrangements led to no significant differences in the subsequent spectral calculation. We also took no account of the Jahn-Teller effects around Ni ions as a first approximation since the dopants themselves are not Jahn-Teller ions.

Theoretical Al and Mg *K* spectra were obtained using the augmented plane-wave and local-orbital (APW+lo) band calculations,[35] where a 1*s* core hole was introduced in the dopant atom. The supercell size was the same as the atomic arrangement calculations. The core-hole to core-hole distance in our calculations was approximately 9 Å. The electron transition probabilities were calculated within the electric-dipole approximation. They were integrated over a $3\times3\times3$ **k** mesh and the final spectrum was broadened by a Gaussian function with a FWHM of 1.00 eV and a Lorentzian function with a FWHM of 0.36 eV so as to approximate the incident-beam width and core-hole lifetime broadening, respectively. The energy-dependent lifetime broadening of the final states was ignored since its effect was not significant for the spectral features near the edge threshold. $R_{\mathrm{MT}}K_{\mathrm{MAX}}$, the parameter for the cutoff of the plane-wave basis was set to 7.0, resulting in sufficient convergence of the spectral shapes. The calculations were run in parallel using eight CPUs of Pentium 4 Core2, which required three to seven days to obtain a theoretical spectrum of one model.

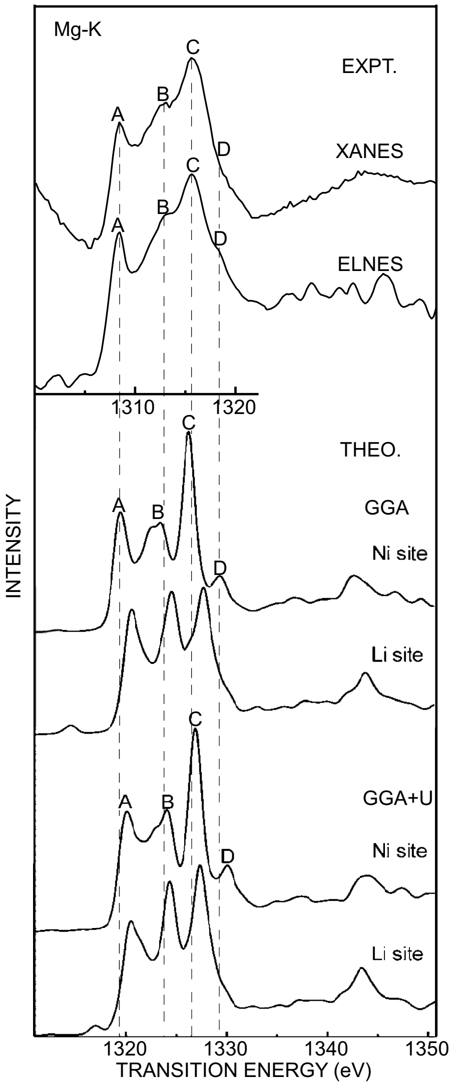

FIG. 1. Experimental Mg *K* ELNES and XANES spectra before the cycling tests (upper) and the corresponding theoretical spectra with Mg substituting for the Ni and Li sites in $LiNiO_2$ (lower figures) by two different calculation schemes. Theoretical transition energy is shifted so that the first peak of the theoretical spectrum for Mg *K* of a reference material (rocksalt MgO) is aligned with that of the corresponding experimental spectrum.

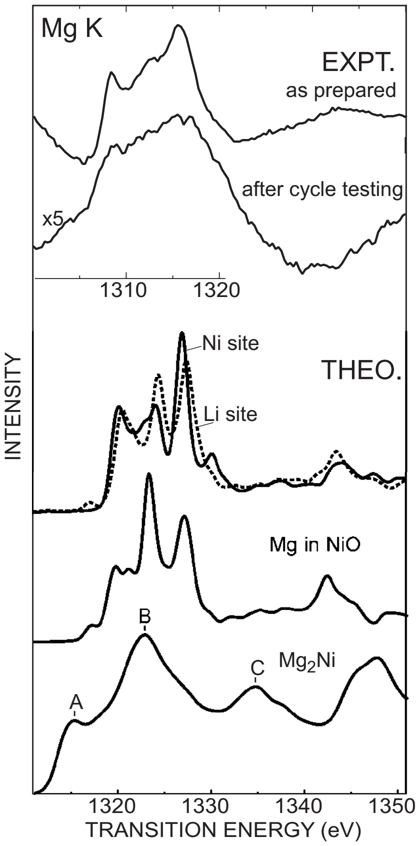

FIG. 2. Experimental Mg *K* XANES of the cathodes before and after the cycling tests (upper) and theoretical spectra of Mg at several possible chemical states (lower).

In order to investigate changes in the ionic bond strength associated with the dopants, the effective charges of the ions, Q, were calculated by the Bader's method, where the electron cloud was assigned topologically to each ion.[36] Since the electron density has to be sufficiently converged with respect to the spherical harmonics ($Y_{l,m}$) expansion prior to this charge assignment, we used a $Y_{l,m}$ up to $l,m=10$.

III. RESULTS

A. Mg *K* spectra

ELNESs from dilute (approximately 1 at. %) elements generally provide very low signal-to-noise ratios (SNRs). The spectrum drifts because of the external stray field and detector/microscope instabilities also significantly smear out the spectral detail for prolonged measurements. In order to overcome these difficulties, we applied a signal restoration procedure based on the Pixon algorithm to the Mg *K* ELNES with a low SNR. The details of this process have already been reported elsewhere.[37,38] The resultant Mg *K* ELNES from the electrode sample before the cycle tests is shown in Fig. 1, together with the corresponding XANES spectrum from the as-synthesized powder for comparison. Peaks A–D of the ELNES and XANES appear at the same positions with similar relative intensities, indicating that there are no significant differences in the chemical states of Mg at the grain surfaces and in-grain regions.

The theoretical spectra of Mg at the Ni site are more consistent with the experimental spectra with respect to the relative intensities and positions of the peaks than those at the Li site irrespective of whether GGA or GGA+U was used. Thus, we conclude that Mg atoms mainly occupy the Ni sites.

Figure 2 compares Mg *K* XANES spectra of as-prepared samples and samples after cycle tests. The spectrum profile from the degraded sample is extended in both the lower (~1305 eV) and higher (~1320 eV) energy directions and its absolute intensities are markedly lowered, compared to those of as-synthesized samples. The lower intensities suggest that a significant amount of Mg atoms was eluted out of the electrode active materials to the electrolytes during the cycle tests. We investigated the theoretical spectra for pos-

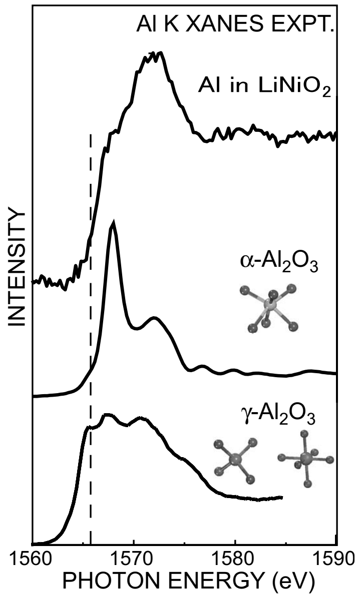

FIG. 3. Al K XANES of the $LiNi_{0.75}Co_{0.15}Al_{0.05}Mg_{0.05}O_2$ powder (top) compared to the experimental XANES spectra of the representative materials in which the corresponding local coordinations of Al are inset.

sible chemical states of the residual Mg, i.e., (i) Mg substituting for Ni in the rocksalt-type NiO and (ii) Mg forming the intermetallic compound Mg_2Ni as a by-product during the cycle tests. A NiO-like structure has actually been observed in the degraded sample,[39] and the fact that the intensity extended to lower energies suggests lower oxidation states of Mg.

The theoretical spectrum of Mg_2Ni (shown at the bottom of Fig. 2) actually reproduces the features extending in both directions of the energy axis, which likely corresponds to those from the degraded sample. We speculate that the actual chemical states of Mg in the degraded sample are a mixture of various states like those shown above, which could give rise to the broadened spectrum observed experimentally. Another possibility is that a part of Mg atoms eluted into the electrolytes, forming organic compounds during the cycle tests because Mg in such organic materials is assumed to be at low oxidation states.

B. Al *K* spectra

Figure 3 compares the experimental Al K XANES from the as-synthesized powder with those of α-Al_2O_3 (a corundum-type structure) and γ-Al_2O_3 (a defective spinel-type structure), giving a rough idea of the chemical environment around Al. α-Al_2O_3 consists of six-coordinated Al (C_{3v} symmetry), whereas γ-Al_2O_3 comprises four- and six-coordinated [having nearly T_d (tetrahedral) and O_h symmetry (octahedral), respectively] Al. In many Al-containing oxides and oxynitrides, Al in tetrahedral coordinations exhibits a characteristic single peak at the spectrum onset (1566 eV in Fig. 3), whereas Al in octahedral coordinations shows a double peak at higher energies (1568 and 1572 eV in Fig. 3),[40–42] and hence experimental Al K XANES indicates that the doped Al should be octahedrally coordinated.

Figure 4 compares the experimental XANES and ELNES spectra with theoretical spectra based on several plausible models. Since Al K ELNES had an even lower signal-to-background ratio than the Mg K ELNES, we conducted a continuous spectrum acquisition, each exposure lasting 30 s and accumulated 100 spectra whose energy shift was computationally realigned by taking the cross correlation between the first and successive recorded spectrum during the measurement.[43] Both XANES and ELNES of the initial sample exhibit two major peaks (A and B), though their relative intensities are slightly different, suggesting that the local environments of the Al in the surface region responsible for XANES (within a depth of approximately 10 nm, estimated from the electron escape depth) would be different from those in the subsurface region.

As previously reported,[39,44] in the cycled electrode sample a NiO-like phase having a rocksalt-type structure evolved. The Al K ELNES of the cycled sample in Fig. 4 was deliberately collected from a region of the NiO-like phase, which exhibits peak B intensity slightly sharper and larger than that of the initial state. Al K-edge ELNES from normal $LiNiO_2$-like regions in the cycled sample is not shown in this figure because it was very similar to that of the initial sample.

For the theoretical models, we found two types of metastable structures for the supercell with Al occupying a Ni site, which have local minima in total energies after structural optimization. We will hereafter refer to them as models 1 and 2 (cf. Fig. 5) and show the theoretical spectra for both. Let us examine the reason why the relative peak intensities of models 1 and 2 exhibit such considerable differences: the angles subtended by O-Al-O are 91.9 and 92.6 (93.2 and 93.6) for models 1 and 2 of GGA+U (GGA), respectively. As the angle increases from the right angle (i.e., as the local coordination of Al deviates further from the O_h symmetry), peak A theoretically tends to show a sharper and larger profile. Peak A of α-Al_2O_3, in which an Al atom is coordinated by six oxygen atoms having a C_{3V} symmetry, actually shows a very sharp and large intensity, as shown in Fig. 3. The previous theoretical studies of Al K and L_{23} ELNES or XANES ascribed the sharp first peak of α-Al_2O_3 to the core-hole effect at the bottom of the conduction band,[45,46] whose wave functions are spatially localized almost within the first nearest neighbors (NNs), whereby a slight change in the bond angle may influence this peak feature significantly.

Returning to the experimental spectra and considering that Al is trivalent, the areal intensity ratio of the two peaks in the XANES and ELNES would be most consistent with the GGA+U results for models 1 and model 2, respectively. However, there is no reason based solely on the spectral features to rule out the possibility that Al occupies the Li site. Since the calculated spectra indicate that the Al in NiO and Al substituting for the Li site would exhibit sharper features of peak B, the observed change in the ELNES suggests that some Al ions in the degraded region may have similar local environments to those Al.

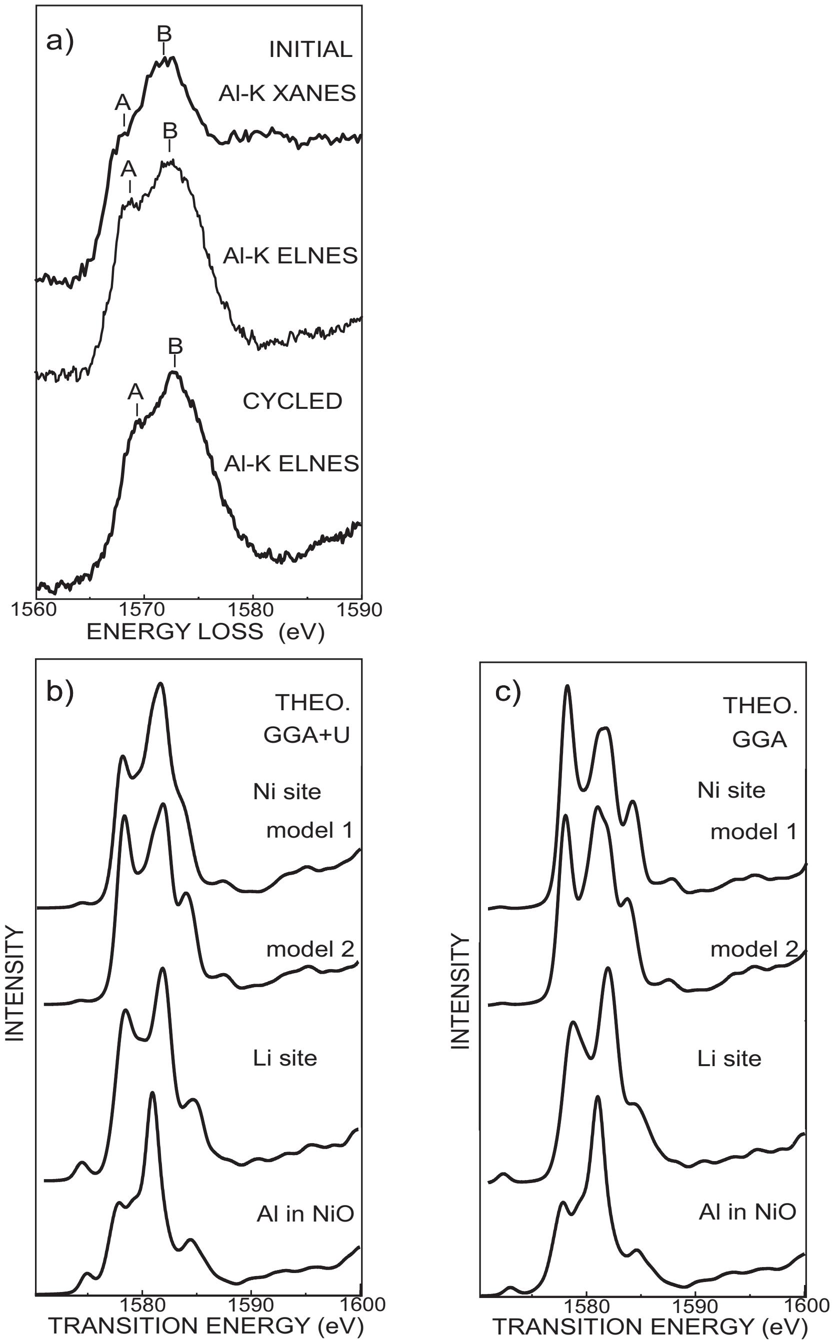

FIG. 4. (a) Experimental Al *K* XANES and ELNES spectra before and after the cycling tests. [(b) and (c)] Corresponding theoretical spectra with Al substituting for the Ni and Li sites in $LiNiO_2$ and with Al substituting for the Ni site in NiO using a different approximation level. Models 1 and 2 in the figures correspond to the two possible metastable structures shown in Fig. 5 (see text for detail). Theoretical transition energy is shifted in the same way as in Fig. 1 using corundum Al_2O_3 as a reference material.

IV. DISCUSSION

A. Atomic arrangements around Mg at Ni sites

The calculated Mg-O bond length is 2.06 Å, which is 4% larger than the calculated Ni-O bond length in undoped $LiNiO_2$ and 2% smaller than the Li-O bond length. The effective charge, *Q*, was assigned 1.4 and 1.3 (1.3 and 1.2), respectively, to the Ni atoms nearest and second nearest to the Mg dopant for the GGA+*U* (GGA) result, indicating a slightly nonuniform charge. Consequently, the Ni-O bond length of the less charged Ni (i.e., the second NN Ni) is 3% larger than that in the undoped $LiNiO_2$. Figure 5(a) shows the calculated atomic positions of the Mg doped, projected in the 001 direction. The oxygen (O_1) bonded to Mg and the oxygen (O_2) bonded to the second NN Ni are displaced outward from the respective cations. These oxygen displacements will affect the lithium diffusion; Fig. 6 shows the LiO_6 octahedrons in $LiMO_2$, each connected by the shared ridge, in which two triangular faces act as the bottlenecks for the lithium migration paths. O_1 and O_2 on the same oxygen plane perpendicular to the *c* axis, being close to each other, alter the lengths of the three sides of the triangles to 3.10, 3.09, and 2.80 Å, whereas the figures are 3.12, 3.12, and 2.90 Å in the theoretically optimized undoped $LiNiO_2$. Considering that the area of the triangle is proportional to the height of the energy barrier for Li migration, the displacements of the O atoms induced by Mg doping could require a higher activation energy for lithium migration.

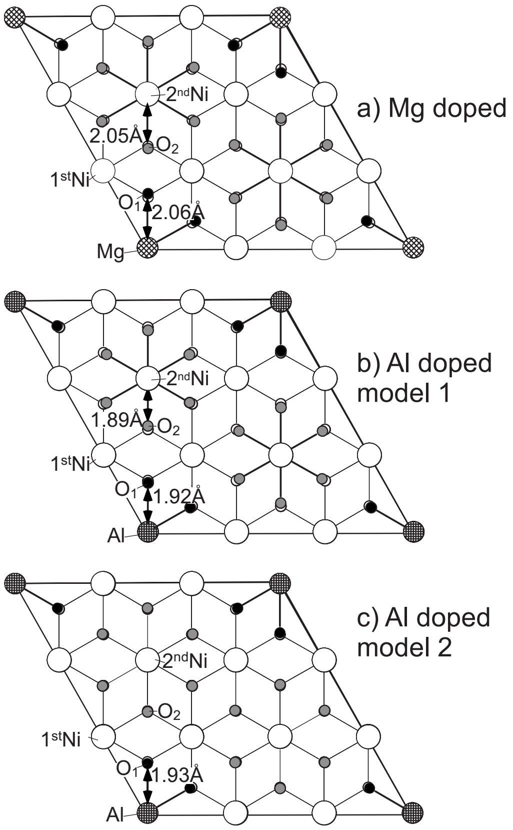

FIG. 5. Calculated atomic arrangements for (a) Mg doped and [(b) and (c)] Al doped: models 1 and 2 of $LiNiO_2$ projected along 001 direction.

B. Atomic arrangements around Al at Ni sites

The calculated atomic positions of models 1 and 2 are shown in Figs. 5(b) and 5(c), respectively. In both models, the Al-O bond lengths are 2% shorter than the Ni-O in bulk $LiNiO_2$. In model 1, O_2 are significantly displaced toward the second NN Ni, parallel to the basal plane. As a result, the Ni-O bonds of the second NN Ni were shortened by 4%. Experimentally, as the aluminum content increases, x-ray diffraction patterns of Al-doped $LiNiO_2$ (Refs. 8 and 14) actually showed line broadening, particularly for the (110) and (113) lines, indicating the local strains in the basal plane. This can be qualitatively explained by the shortened Ni-O bonds due to the oxygen displacement in the supercell of model 1.

The lengths of the three sides of the triangular faces composed of three adjacent O_2 are 3.10, 3.10, and 2.70 Å in model 1, which have the smallest triangle area among the calculated model. Because of the area of the triangles, the Li mobility would increase in the order undoped > Mg-doped > Al-doped $LiNiO_2$, which is consistent with the fact that Al doping by a larger amount causes, even at the initial stage of the cycle tests, high electrical resistance.[20]

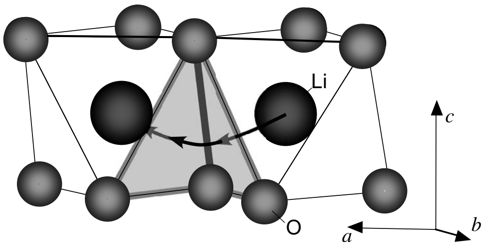

FIG. 6. Possible migration path of Li ions (curved arrows). Gray triangles presumably act as bottlenecks in the path.

TABLE I. Effective charge, Q, of the dopants and their first nearest-neighbor oxygen.

System	Ni site	Li site	First NN O
Mg doped	1.5, 1.6[a]	1.6	−1.1, −1.2 [a] (Ni site) −1.1 (Li site)
Al doped	2.1	2.1	−1.1, −1.2 [a]
Reference $LiNiO_2$ bulk	1.3	0.7	−1.0

[a] The first and second values correspond to the GGA and GGA+U results, respectively.

It is interesting that the first and second NN Ni of the doped Al have effective charges of 1.3 and 1.5 (1.2 and 1.3) for model 1 of the GGA+U (GGA) result, respectively, indicating a nonuniform charge distribution with a trend opposite to that of the case of Mg doping. The calculated effective charges of the dopants and the constituent ions in the $LiNiO_2$ bulk are listed in Table I. Al always exhibits an oxidation state much higher than Mg and Ni, irrespective of the occupying site. In terms of the conventional picture of ionic crystals, when Ni is replaced by Al having a smaller ion size and higher oxidation state, the second NN Ni tends to take a higher oxidation state (smaller ionic radius), which releases the lattice stress due to the mismatch between the different ionic sizes. In fact, the calculated total energy of model 1 is lower than that of model 2 by 0.3 (0.5) eV per Al atom for the GGA+U (GGA) result.

C. Local chemical bonding changes caused by the dopants

In order to investigate the local chemical bonding changes caused by the dopants, the ionic bond strength between ions i and j was evaluated by I_{ij} defined as

$$I_{ij} = -\frac{Q_i Q_j}{r_{ij}}, \tag{2}$$

where Q_i is the effective charge of the ion i and r_{ij} is the distance between ions i and j. The calculated I_{ij} values of the several ion pairs of interest are shown in Fig. 7 for the supercells of Mg substituting for the Ni site and Al substituting for the Ni site (models 1 and 2), whose theoretical K-shell excited spectra were the most consistent with the experimental spectra. They are plotted with respect to the distances, d, between the dopants and the center of the corresponding bonds as illustrated in the inset.

As for the Li-O bonds, the dopants increase their I_{ij} values slightly, irrespective of the dopants and the models. For the Ni-O pairs, the bond strengths in the NiO_2 layer are significantly increased within a distance of 3–4 Å from the dopants. The Al-O bond has a particularly large I_{ij}, and the doped Al in model 1 also strengthens the bond between the

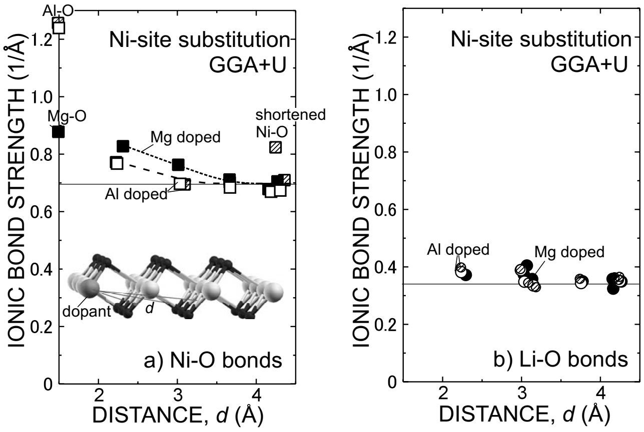

FIG. 7. Calculated ionic bond strengths, I_{ij} (i=O and j=Ni or Li) in Eq. (2) for the Mg doped (filled), and models 1 (hatched) and 2 (unfilled) of the Al-doped cases. The horizontal thin lines indicate the values in the undoped $LiNiO_2$. (a) Ni-O bonds. (b) Li-O bonds.

second NN Ni and O atoms at $d=4.3$ Å. On the other hand, the Mg doping results in larger I_{ij}'s than Al doping for the Ni-O bonds of $d=2-4$ Å.

Previous TEM observations reported that NiO-like cubic phases were coproduced during the charge/discharge reactions and presumed that these phases were strongly related to the fading of the battery properties.[39] The present theoretical results suggest that the dopants prevent the NiO_2 layers in Li_xNiO_2 from collapsing to form NiO-like phases by the reinforced neighboring ionic bonds. This effect is more conspicuous for Mg because it induces stronger and more spatially homogeneous Ni-O bonds than Al does.

Chang *et al.*[1] reported the electrochemical properties of Li_xNiO_2 upon systematic charge-discharge cycles: the electrodes of $0.3<x<1$ exhibited no significant degradation after the cycles irrespective of whether Mg was doped or not, whereas for the $x<0.3$ electrodes, only the nondoped electrodes were appreciably degraded. They expected that the doped Mg at the charged state prevented the following decomposition reaction:

$$Li_{x<0.3}NiO_2 \rightarrow LiNi_2O_4 + O_2(g) + NiO. \qquad (3)$$

They discussed that the following two mechanisms can suppress the reaction: (1) the presence of inert species (Mg^{2+} and Ni^{4+}) on the transition-metal site helps us to prevent overcharging during the charging process. (2) The doped Mg reinforced the interatomic bonding in the NiO_2 layers. The present analysis supports the second mechanism.

Let us add a few words about the degree of the covalency. In the topological analysis of the charge density $\rho(\mathbf{r})$, ρ, and its Laplacian $\Delta\rho$ at a saddle in $\rho(\mathbf{r})$ along the bond path could be used to evaluate the degree of the covalency. In our models, $\Delta\rho$ values for the Ni-O and Li-O bonds were positive, indicating that they were ionic. ρ at a saddle of the Ni-O bonds near neighbor to the dopants were larger than those in the undoped $LiNiO_2$. However their increments were smaller than one-half of those seen in I_{ij}. These things validate with our ionic model for the chemical bonding changes caused by the dopants.

V. SUMMARY

Local atomic structures and chemical bonding around the dopants Mg and Al in the Li battery cathode material have been investigated by their *K*-shell excited spectra and first-principles calculations. The main results can be summarized as follows: (1) Mg *K* spectra of the initial sample indicated that the Mg atoms mainly occupied the Ni sites. The markedly lowered intensities of Mg *K* XANES of the cycled sample suggested that a significant amount of Mg was eluted out of the electrode active materials to the electrolytes during the cycle tests. Its profile was broader and extended to both lower and higher energies. It is concluded from the theoretical Mg *K* spectra that the actual chemical states of Mg in the degraded sample should not only be substitutional sites in the cathode active material but also low oxidation states in byproducts of the cycle test. (2) Although Al *K* XANES and ELNES had two major peaks (A and B), the relative intensities of the initial sample were slightly different, which suggests that the local environments of the Al in the surface region responsible for XANES would be different from those in the subsurface region. Al *K* XANES was most consistent with the theoretical spectrum of Al whose second-nearest-neighbor Ni was preferentially oxidized with shorter Ni-O bonds. Al *K* ELNES collected from the degraded region in the cycled sample showed a sharper peak B, which is most consistent with Al in NiO or Al in the Li site. (3) In the energetically stable atomic arrangements around the dopants Mg and Al, the first nearest oxygen atoms and those coordinating to the second-nearest Ni atoms were significantly displaced, compared to the undoped $LiNiO_2$. Assuming that the triangular areas constructed by those displaced oxygen atoms act as bottlenecks for Li migration, the mobility of Li would increase in the order undoped>Mg-doped>Al-doped $LiNiO_2$. (4) Ionic bond strengths were evaluated using the calculated effective charges and bond lengths. Mg induced stronger and more spatially homogeneous Ni-O bonds than Al did, indicating that Mg would be more effective for preventing the fading of the battery properties by reinforcing the interatomic bonding in the NiO_2 layers.

ACKNOWLEDGMENTS

The present work was partly supported by Grants-in-Aid for Scientific Research of MEXT, Japan [Kiban-Kenkyu A and Priority Area (Grant No. 474) "Atomic Scale Modification"] and JSPS [Wakate B (Grants No. 16760531 and No. 18760493)].

*Author to whom correspondence should be addressed; k-tatsumi@nucl.nagoya-u.ac.jp

[1] C. C. Chang, J. Y. Kim, and P. N. Kumta, J. Electrochem. Soc. **147**, 1722 (2000).

[2] C. C. Chang, J. Y. Kim, and P. N. Kumta, J. Power Sources **89**, 56 (2000).

[3] C. Pouillerie, L. Croguennec, Ph. Biensan, P. Willmann, and C. Delmas, J. Electrochem. Soc. **147**, 2061 (2000).

[4] C. Pouillerie, F. Perton, Ph. Biensan, J. P. Peres, M. Broussely, and C. Delmas, J. Power Sources **96**, 293 (2001).

[5] A. R. Naghash and J. Y. Lee, Electrochim. Acta **46**, 2293 (2001).

[6] B. V. R. Chowdari, G. V. Subba Rao, and S. Y. Chow, Solid State Ionics **140**, 55 (2001).

[7] A. Yu, G. V. Subba Rao, and B. V. R. Chowdari, Solid State Ionics **135**, 131 (2000).

[8] T. Ohzuku, A. Ueda, and M. Kouguchi, J. Electrochem. Soc. **142**, 4033 (1995).

[9] M. Y. Song, R. Lee, and I. Kwon, Solid State Ionics **156**, 319 (2003).

[10] Y.-I. Jang, B. Huang, H. Wang, G. R. Maskaly, G. Ceder, D. R. Sadoway, Y.-M. Chiang, H. Liu, and H. Tamura, J. Power Sources **81-82**, 589 (1999).

[11] A. D'Epifanio, F. Croce, F. Ronci, V. R. Albertini, E. Traversa, and B. Scrosati, Phys. Chem. Chem. Phys. **3**, 4399 (2001).

[12] S.-H. Kang, J. Kim, M. E. Stoll, D. Abraham, Y. K. Sun, and K. Amine, J. Power Sources **112**, 41 (2002).

[13] M. Guilmard, L. Croguennec, D. Denux, and C. Delmas, Chem. Mater. **15**, 4476 (2003).

[14] S. H. Park and Y.-K. Sun, J. Power Sources **119-121**, 161 (2003).

[15] S. H. Park, K. S. Park, Y. K. Sun, K. S. Nahm, Y. S. Lee, and M. Yoshio, Electrochim. Acta **46**, 1215 (2001).

[16] K. K. Lee, W. S. Yoon, K. B. Kim, K. Y. Lee, and S. T. Hong, J. Power Sources **97-98**, 308 (2001).

[17] X.-J. Zhu, H.-X. Liu, X.-Y. Gan, M.-H. Cao, J. Zhou, W. Chen, Q. Xu, and S.-X. Ouyang, J. Electroceram. **17**, 645 (2006).

[18] P. Kalyani, N. Kalaiselvi, N. G. Renganathan, and M. Raghavan, Mater. Res. Bull. **39**, 41 (2004).

[19] H. Kondo, Y. Takeuchi, T. Sasaki, S. Kawauchi, Y. Itou, O. Hiruta, M. Yonemura, T. Kamiyama, and Y. Ukyo, J. Power Sources **174**, 1131 (2007).

[20] J. Kim, B. H. Kim, Y. H. Baik, P. K. Chang, H. S. Park, and K. Amine, J. Power Sources **158**, 641 (2006).

[21] S. Madhavi, G. V. Subbao Rao, B. V. R. Chowdari, and S. F. Y. Li, Solid State Ionics **152-153**, 199 (2002).

[22] C. Julien, G. A. Nazri, and A. Rougier, Solid State Ionics **135**, 121 (2000).

[23] Y. Koyama, I. Tanaka, and H. Adachi, Adv. Quantum Chem. **42**, 145 (2003).

[24] F. Zhou, M. Cococcioni, C. A. Marianetti, D. Morgan, and G. Ceder, Phys. Rev. B **70**, 235121 (2004).

[25] C. C. Chang, O. I. Velikokhatnyi, and P. N. Kumta, J. Electrochem. Soc. **151**, J91 (2004).

[26] T. Amriou, A. Sayede, B. Khelifa, C. Mathieu, and H. Aourag, J. Power Sources **130**, 213 (2004).

[27] K. Suzuki, Y. Kuroiwa, S. Takami, M. Kubo, and A. Miyamoto, Appl. Surf. Sci. **189**, 313 (2002).

[28] Y. Itou and Y. Ukyo, J. Power Sources **146**, 39 (2005).

[29] J. P. Perdew, K. Burke, and M. Ernzerhof, Phys. Rev. Lett. **77**, 3865 (1996).

[30] V. I. Anisimov, I. V. Solovyev, M. A. Korotin, M. T. Czyzyk, and G. A. Sawatzky, Phys. Rev. B **48**, 16929 (1993).

[31] S. L. Dudarev, G. A. Botton, S. Y. Savrasov, C. J. Humphreys, and A. P. Sutton, Phys. Rev. B **57**, 1505 (1998).

[32] P. E. Blochl, Phys. Rev. B **50**, 17953 (1994).

[33] G. Kresse and D. Joubert, Phys. Rev. B **59**, 1758 (1999).

[34] G. Kresse and J. Furthmuller, Phys. Rev. B **54**, 11169 (1996).

[35] P. Blaha, K. Schwarz, G. K. H. Madsen, D. Kvasnicka, and J. Luitz, *WIEN2K, An Augmented Plane Wave Plus Local Orbitals Program for Calculating Crystal Properties* (Karlheinz Schwarz, Techische Universitat Wien, Austria, 2001).

[36] R. F. W. Bader, *Atoms in Molecules—A Quantum Theory* (Oxford University Press, Oxford, 1990).

[37] S. Muto, R. C. Puetter, and K. Tatsumi, J. Electron Microsc. **55**, 215 (2006).

[38] S. Muto, K. Tatsumi, R. C. Puetter, T. Yoshida, Y. Yamamoto, and Y. Sasano, J. Electron Microsc. **55**, 225 (2006).

[39] D. P. Abraham, R. D. Twesten, M. Batasubramanian, J. Kropf, D. Fischer, J. McBreen, I. Petrov, and K. Amine, J. Electrochem. Soc. **150**, A1450 (2003).

[40] K. Tatsumi, S. Muto, Y. Yamamoto, H. Ikeno, S. Yoshioka, and I. Tanaka, Ultramicroscopy **106**, 1019 (2006).

[41] Y. Yamamoto, K. Tatsumi and S. Muto, Mater. Trans., JIM **48**, 2590 (2007).

[42] K. Tatsumi, T. Mizoguchi, S. Yoshioka, T. Yamamoto, T. Suga, T. Sekine, and I. Tanaka, Phys. Rev. B **71**, 033202 (2005).

[43] Y. Sasano and S. Muto (unpublished).

[44] Y. Sasano, K. Tatsumi, S. Muto, T. Sasaki, K. Horibuchi, Y. Takeuchi, and Y. Ukyo, *212th Electrochemical Society Meeting Abstracts* (Curran Associates, NY, 2007), p. 664.

[45] I. Tanaka and H. Adachi, Phys. Rev. B **54**, 4604 (1996).

[46] S. Nufer, T. Gemming, C. Elsasser, S. Kostlmeier, and M. Ruhle, Ultramicroscopy **86**, 339 (2001).